Electronic Supplementary Material (ESI) for Nanoscale.

Toward high-performance refractive index sensor using single Au nanoplate-on-mirror nanocavity

Qifa Wang [a], Liping Hou [a], Chenyang Li [a], Hailin Zhou [a], Xuetao Gan [a], Kaihui Liu [b], Fajun Xiao *[a] and Jianlin Zhao *[a]

[a]Key Laboratory of Light Field Manipulation and Information Acquisition, Ministry of Industry and Information Technology, and Shaanxi Key Laboratory of Optical Information Technology, School of Physical Science and Technology, Northwestern Polytechnical University, Xi'an 710129, China

[b]State Key Laboratory for Mesoscopic Physics, Collaborative Innovation Centre of Quantum Matter, School of Physics, Peking University, Beijing 100871, China

*Corresponding author: fjxiao@nwpu.edu.cn and jlzhao@nwpu.edu.cn

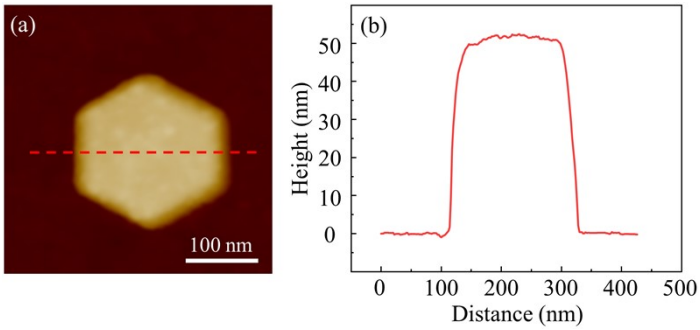

Fig. S1. (a) AFM height image of an individual hexagonal Au NPoM. (b) Height profile extracted along the dashed line indicated in (a).

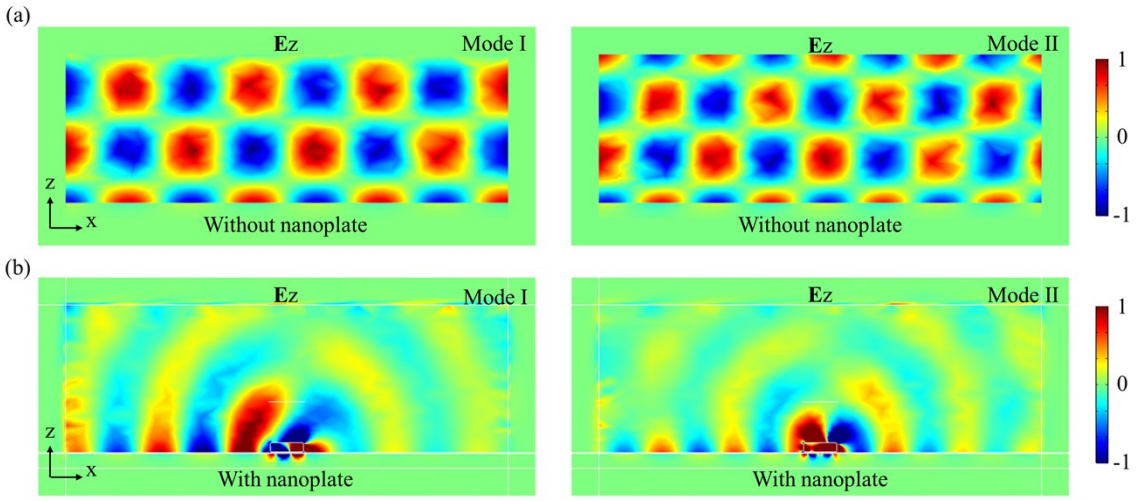

Fig. S2. Distribution of the normalized real part of electric field component **E**z (a) without and (b) with Au nanoplate siting on the Au film coated by a 5 nm-thick Al_2O_3 layer. Here, the left and right column are for field distributions of mode I and II, respectively.

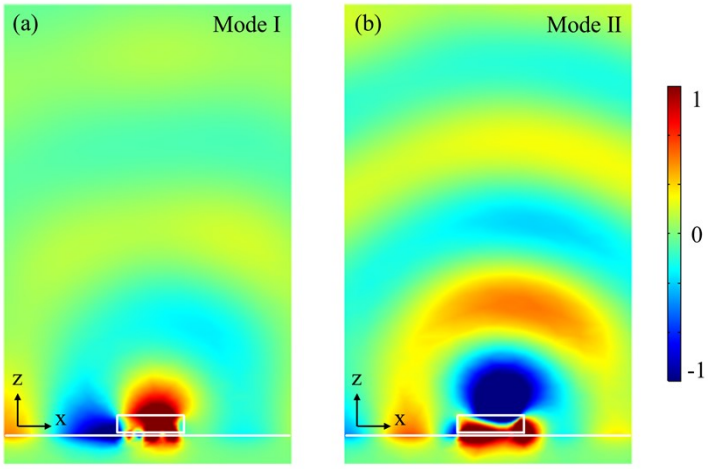

Fig. S3. Distribution of the normalized real part of magnetic field component $\mathbf{H}_y$ for (a) mode I and (b) mode II of the hexagonal Au NPoM (g=5 nm, d=180 nm) in water environment.

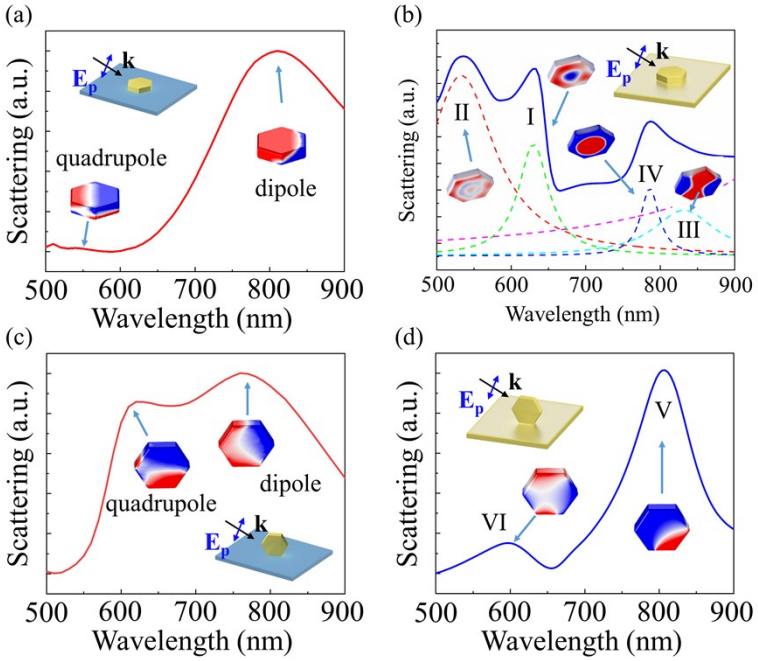

Fig. S4. Simulated scattering spectra of Au nanoplate (*d*=185 nm) on (a) SiO_2/Si substrate and (b) Al_2O_3 spacer/Au film when illuminated by the p-polarized beam with an incidence angle of 70°. Simulated scattering spectrum of vertical Au nanoplate (*d*=185 nm) on (c) SiO_2/Si substrate and (d) Al_2O_3 spacer/Au film under the illumination of p-polarized beam with an incidence angle of 70°. The inset shows the charge distributions at corresponding resonance peaks.

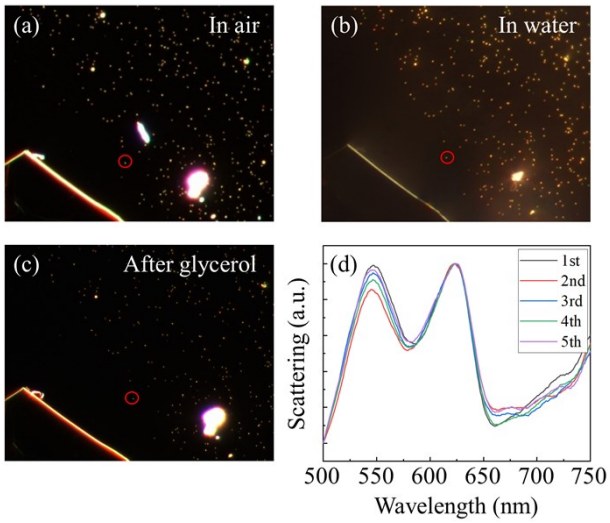

Fig. S5. Dark-field images of the NPoM sensor in (a) air, (b) water, and (c) in air drying after immersing of glycerol solutions with various mass fractions followed by several rinses with deionized water. (d) Scattering spectra of the hexagonal Au NPoM sensor chosen by red circle after repeatedly immersing of glycerol solutions followed by several rinses with deionized water and redrying.

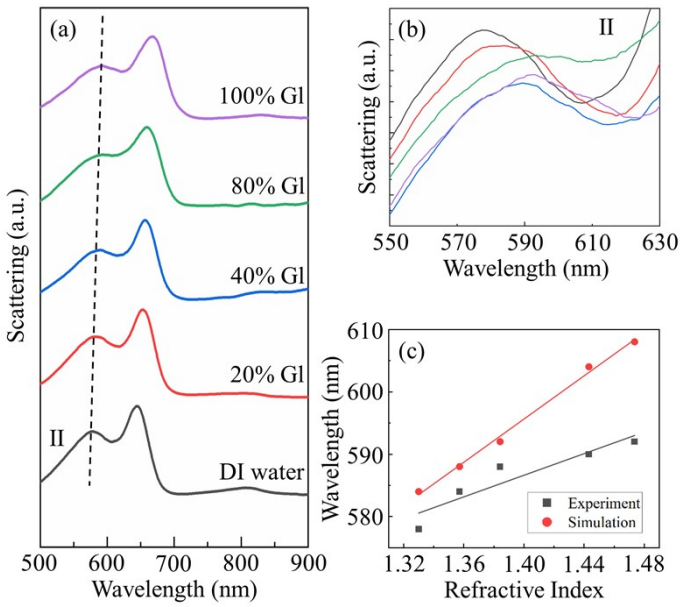

Fig. S6. (a) Experimental scattering spectra of the hexagonal Au NPoM (g = 5 nm, d = 180 nm) in solutions with different glycerol mass fractions, where the black dashed line indicates the peak shift of mode II. (b) Zoom-in spectra of mode II in a). (c) Resonance wavelength of mode II as a function of the refractive index of surrounding solution, where the black and red dots are for the experiment and simulation results, respectively.

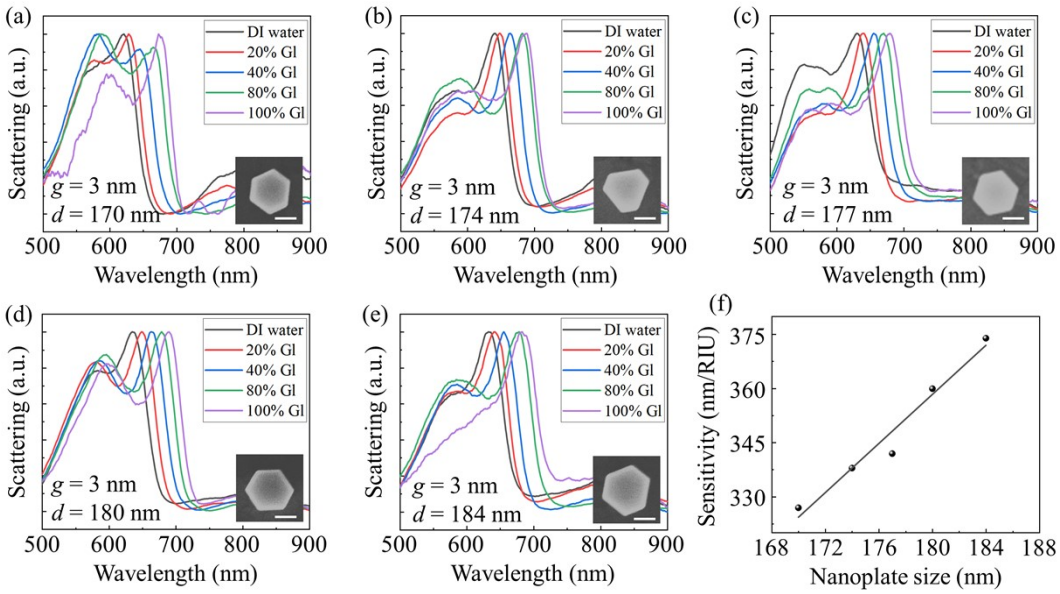

Fig. S7. Measured scattering spectra of NPoM (*g*=3 nm) with the nanoplate size of (a) 170 nm, (b) 174 nm, (c) 177 nm, (d) 180 nm, and (e) 184 nm in glycerol solutions with different mass fractions. (f) Sensitivity of NPoM sensor (*g*=3 nm) versus nanoplate size. The insets of (a)-(e) show the SEM images of the nanoplates. The scale bar is 100 nm.

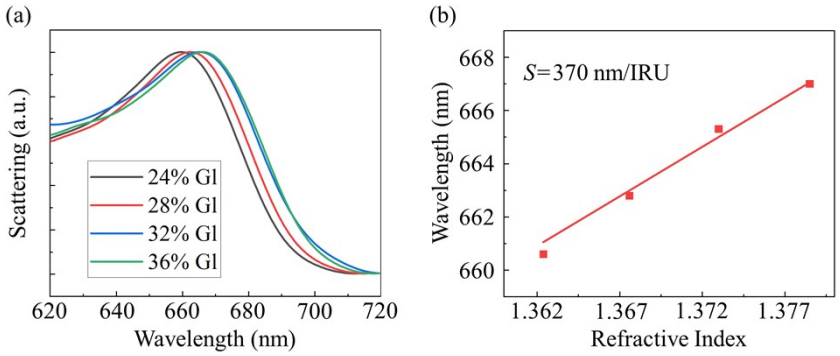

Fig. S8. (a) Refractive index sensing using mode I of the hexagonal Au NPoM (g=3 nm, d=180 nm) in glycerol solutions with mass fractions of 24%, 28%, 32%, and 36%, whose refractive indices were taken as 1.3624, 1.3676, 1.3730, and 1.3785, respectively. (b) Resonance wavelength of mode I as a function of the refractive index of surrounding solution. The refractive index sensitivity obtained from the linear regression analysis (the solid lines) is labeled in this figure.

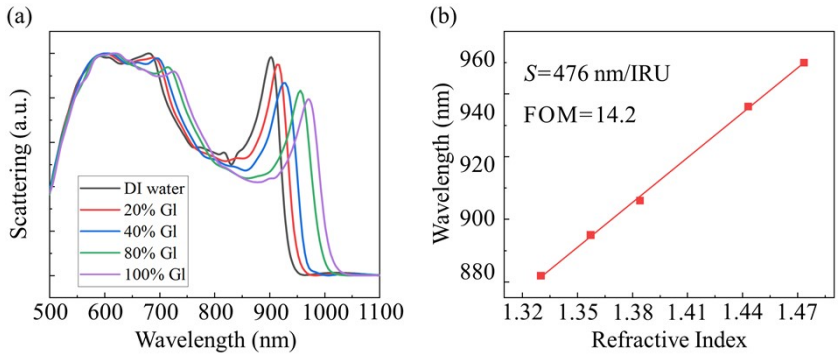

Fig. S9. (a) Simulated scattering spectra of the hexagonal Au NPoM (g=2 nm, d=280 nm) in solutions with different glycerol mass fractions. (b) Resonance wavelength of mode I as a function of the refractive index of surrounding solution. The refractive index sensitivity obtained from the linear regression analysis (the solid lines) as well as the FOM are labeled in this figure.